11-15-2016

Fast Motions of Key Methyl Groups in Amyloid-beta Fibrils

Liliya Vugmeyster
liliya.vugmeyster@ucdenver.edu

Dmitry Ostrovsky

Matthew A. Clark

Isaac B. Falconer

Gina L. Hoatson
College of William and Mary, gina@physics.wm.edu

See next page for additional authors

Recommended Citation

Vugmeyster, Liliya; Ostrovsky, Dmitry; Clark, Matthew A.; Falconer, Isaac B.; Hoatson, Gina L.; and Qiang, Wei, Fast Motions of Key Methyl Groups in Amyloid-beta Fibrils (2016). *BIOPHYSICAL JOURNAL*, 111(10). 10.1016/j.bpj.2016.10.001

Biophysical Journal
Article

Biophysical Society

Fast Motions of Key Methyl Groups in Amyloid-β Fibrils

Liliya Vugmeyster,[1,*] Dmitry Ostrovsky,[2] Matthew A. Clark,[3] Isaac B. Falconer,[1] Gina L. Hoatson,[4] and Wei Qiang[5]
[1]Department of Chemistry and [2]Department of Mathematics, University of Colorado at Denver, Denver, Colorado; [3]Department of Chemistry, University of Alaska Anchorage, Anchorage, Alaska; [4]Department of Physics, College of William and Mary, Williamsburg, Virginia; and [5]Department of Chemistry, Binghamton University, Binghamton, New York

ABSTRACT Amyloid-β (Aβ) peptide is the major component of plaques found in Alzheimer's disease patients. Using solid-state ^{2}H NMR relaxation performed on selectively deuterated methyl groups, we probed the dynamics in the threefold symmetric and twofold symmetric polymorphs of native Aβ as well as the protofibrils of the D23N mutant. Specifically, we investigated the methyl groups of two leucine residues that belong to the hydrophobic core (L17 and L34) as well as M35 residues belonging to the hydrophobic interface between the cross-β subunits, which has been previously found to be water-accessible. Relaxation measurements performed over 310–140 K and two magnetic field strengths provide insights into conformational variability within and between polymorphs. Core packing variations within a single polymorph are similar to what is observed for globular proteins for the core residues, whereas M35 exhibits a larger degree of variability. M35 site is also shown to undergo a solvent-dependent dynamical transition in which slower amplitude motions of methyl axes are activated at high temperature. The motions, modeled as a diffusion of methyl axis, have activation energy by a factor of 2.7 larger in the twofold compared with the threefold polymorph, whereas D23N protofibrils display a value similar to the threefold polymorph. This suggests enhanced flexibility of the hydrophobic interface in the threefold polymorph. This difference is only observed in the hydrated state and is absent in the dry fibrils, highlighting the role of solvent at the cavity. In contrast, the dynamic behavior of the core is hydration-independent.

INTRODUCTION

Amyloid-β (Aβ) peptide is the major component of plaques found in Alzheimer's disease patients. The most abundant form of this peptide, A$\beta_{1\text{-}40}$, has been a subject of multiple studies and has been shown to exist in multiple polymorphs that differ in their levels of cytotoxicity (1–13). In particular, structural models are available for the twofold and threefold polymorphs that can be grown under different conditions, which differ principally in whether or not the fibrils get agitated during growth (10). The cytotoxicity of the threefold polymorph was found to be significantly higher than that of the twofold (10). In addition to native polymorphs of Aβ, several mutants have been found in plaques of patients. Of particular interest to this work is the D23N "Iowa" mutation, implicated in an early onset of the disease (5). From the structural standpoint it is different from the native Aβ in that it can form thermodynamically metastable protofibrils (14). Whereas the native Aβ can form only parallel β-sheet structures, the protofibrils of D23N consist of antiparallel β sheets (12,15).

Although multiple studies have been devoted to structural investigations (7,10–12,15–23), investigations of dynamics of Aβ remain relatively sparse (24), partially because of the difficulties of obtaining site-specific resolution in these noncrystalline samples. However, the knowledge of the conformational ensemble and its difference between various polymorphs, protofibrils, and oligomers is expected to play an important role in understanding the molecular basis of cytotoxic behavior of Aβ (25). We have previously employed ^{2}H static line shape measurements in combination with single-site labeling to probe motions in the μs-to-ms timescale range in the hydrophobic core of Aβ as well as the hydrophobic interface defined by M35 contacts (Fig. 1). Based on the structural models, the relative orientation of M35 contacts in different polymorphs can play an important role in defining the water-accessible hydrophobic core cavity, implicated by x-ray, cryo-EM, solid-state NMR, and molecular dynamics (MD) simulations (17,23,26–29). According to the structural models (15), M35 is right at the edge of the β-sheet core region in

Submitted August 3, 2016, and accepted for publication October 5, 2016.
*Correspondence: liliya.vugmeyster@ucdenver.edu
Editor: Jane Dyson
http://dx.doi.org/10.1016/j.bpj.2016.10.001

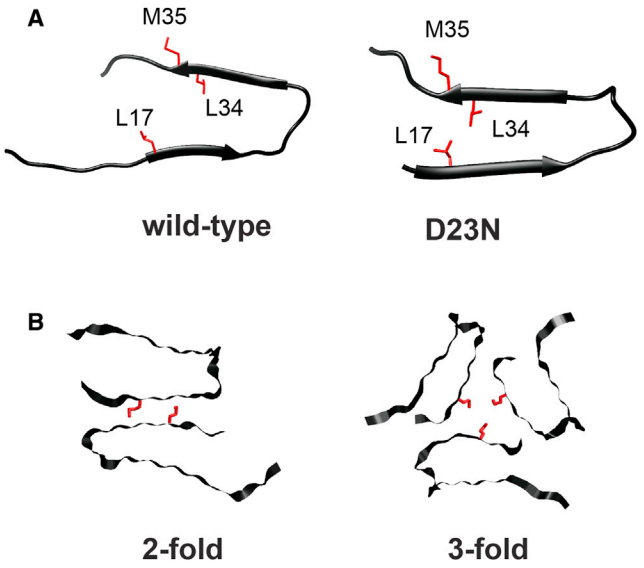

FIGURE 1 (*A*) Ribbon diagram corresponding to monomeric units of the wild-type Aβ_{1-40} (PDB: 2LMN, twofold polymorph) and D23N mutant (PDB: 2LNQ), with the side chains investigated in this work in red. (*B*) Quaternary structures of the twofold (PDB: 2LMN) and threefold symmetric polymorph (PDB: 2LMP) with the side chain of M35 in red are shown. To see this figure in color, go online.

the protofibrils, whereas the core extends to the C-terminal residues in the wild-type Aβ.

We have previously shown that the hydrophobic core is highly dynamic with motions of methyl axes persisting down to at least 200 K (30). Based on molecular modeling and comparison with results for globular proteins, we have argued that low activation energies for rotameric jumps are the primary source that drives the persistence of the dynamics of methyl axes on the μs-ms timescale. Further, we have seen that the dynamics of the hydrophobic core on this timescale is independent of solvation, in sharp contrast to what has been observed for globular proteins (31). However, the M35 site defining the hydrophobic cavity exhibited strong hydration dependence, implying water accessibility. This was seen for both the twofold and the threefold polymorphs. Further, we have observed morphology dependence for the hydrophobic core residues, but not for the hydrophobic water-accessible cavity. The later result is somewhat surprising as, based on the structures, the environment around M35 methyl groups is clearly different in the two polymorphs. Thus, it is possible that the differences in environment manifest themselves over a different timescale range.

The goal of this work is to probe faster timescale motions, in the ps-to-ns range to obtain a more global overview of methyl group dynamics in Aβ. Methyl group dynamics at these timescales are a sensitive probe of overall core packing (32–39) and its variations both within a chosen polymorph and between different polymorphs. An ability to characterize packing variations provides a unique opportunity to assess the degree of variability of the conformational ensemble in the fibrils and compare with what is observed for globular proteins. Further, hydrated globular proteins are known to undergo dynamical transitions upon heating from cryogenic temperatures to physiological range (34,40–45). The transition at ~250–200 K is generally described as activation of large amplitude motions coupled to the solvent (40,46–50). The occurrence of the dynamical transition is generally related to the onset of biological functions (34,51,52). An important question arises: Do fibrils undergo a similar dynamic transition?

By investigating methyl groups at key locations, we obtain insights into these questions. The chosen hydrophobic core sites L17 and L34 as well as M35 has been shown to be essential in defining not only intramolecular, but also intermolecular contacts (10,12,15,53–55). M35 residue is also the focus of many experimental and computational studies because of its role in defining the hydrophobic cavity (17,27–29). We probe the twofold and threefold native polymorphs and the D23N protofibrils using deuterium relaxation measurements (T_{1Z}, Zeeman order, and T_{1Q}, quadrupolar order) on selectively labeled samples. A wide temperature range between 310–140 K is the key for obtaining quantitative information on core packing and dynamical transitions. Interestingly, the dynamics on ps-ns timescale reveals differences between the twofold and threefold polymorphs not only at the hydrophobic core sites, but also at the M35 site, which was not seen through the line shape experiments, thus underscoring the role of local environment in different timescale ranges.

MATERIALS AND METHODS

Preparation of A$\beta_{1\text{-}40}$ peptide and D23N mutant

The native and D23N mutant proteins were prepared using solid-state peptide synthesis (performed by Thermofisher Scientific, Rockford, IL). Fluorenylmethyloxycarbonyl (FMOC)-leucine-5,5,5-d_3 was purchased from Cambridge Isotopes Laboratories (Andover, MA) and FMOC-Metionine-d_3 from CDN Isotopes (Pointe-Claire, Quebec, Canada). The native sequence is DAEFRHDSGYEVHHQKLVFFAEDVGSNKGAIIGLMVGGVV. The peptides were purified by reversed-phase HPLC and their identity and purity was confirmed by mass spectrometry and reversed-phase HPLC. The resulting peptides had isotopic labels in only one chosen residue.

Preparation of the fibrils

The fibrils of the wild-type Aβ were prepared as described in detail in (30) and based on protocols established in (10,56). The main difference in preparation between the twofold and threefold symmetric polymorphs is in the agitation/sonication patterns of the seeds: for the twofold polymorph, sonication was performed every 3 to 4 h and the growth occurred under agitated conditions. For the threefold variant, sonication was performed at 24 h with the growth occurring under quiescent conditions. The bulk fibrils were pelleted by centrifuging at 300,000 g for 3 h, followed by resuspending the pellets in the buffer and a second round of centrifugation. The washing procedure was done to suppress the signal due to the natural abundance of ^{2}H in the DMSO solvent (used for dissolving the peptide) to the level under 0.1%. Fibril pellets were resuspended in deionized water, rapidly frozen with liquid nitrogen, and lyophilized. Preparation of the D23Nprotofibrils

with antiparallel β-sheet structure utilized a two-step seeding/filtration cycle that takes advantage of the differences in fibril formation rate between the parallel and antiparallel structures (12). The resulting morphologies were confirmed with transmission electron microscopy imaging (Fig. S1 in the Supporting Material).

Hydration and preparation of NMR sample

A hydrated state with water content of 200% by weight was achieved by either one of the following two ways, and we have confirmed that the results do not depend on the chosen strategy. The first strategy involved exposing lyophilized powder to water vapor in a sealed chamber at 25°C until the water content reached saturating levels corresponding to ~40% by weight (~12–16 h was sufficient to achieve this), followed by pipetting the remaining water using deuterium depleted H_2O. The second strategy involved pipetting in all water as deuterium depleted H_2O and allowing the sample to equilibrate for 12–36 h. The samples were packed in 5 mm NMR tubes (cut to 21 mm length) using teflon tape to center the sample volume in the coil of the NMR probe. The amount of material packed varied from 9–15 mg for leucine-labeled peptides to 22–32 mg for methionine-labeled ones.

NMR spectroscopy

Data were collected on 17.6 and 9.4 T spectrometers equipped with static deuteron probes. T_{1Z} (Zeeman order) measurements under static conditions were performed by the inversion recovery sequence for relaxation times above 90 ms and saturation recovery sequence for shorter times. T_{1Q} (quadrupolar order) measurements were performed using Broadband Jeener-Broekaert pulse sequence (57,58). All measurements on the 9.4 T spectrometer were performed using quadrupolar echo detection scheme, whereas for the measurements on the 17.6 T spectrometer the multiple echo acquisition detection scheme (QCPMG) was utilized (59). Briefly, QCPMG detection breaks the powder pattern spectrum into a series of spikes that roughly follow the shape of the powder pattern. Unlike magic angle spinning, QCPMG detection does not suppress relaxation anisotropy (60). The durations of 90° pulses were between 2.0–3.0 μs. Ten to fifteen QCPMG echoes were collected with either 104 or 52 μs pulse spacing, corresponding to QCPMG spikelets (sidebands) spaced at 10 or 20 kHz intervals, respectively. The number of scans ranged from 128 to 2048 depending on the signal-to-noise ratio in each sample, as well as the precision of the data needed to define nonexponential decays. Seven to nine relaxation delays were collected. Relaxation data are reported for the spikelets corresponding to major singularities. Spectra were processed using 1 kHz exponential line broadening.

Temperature calibration was performed by recording static lead nitrate line shapes (61) and using the freezing point of D_2O, 3.8°C, as the fixed point for the calibration.

Theoretical background

Zeeman T_{1Z} and quadrupolar order T_{1Q} relaxation rates are given by the following (36,62):

$$\frac{1}{T_{1Z}} = \frac{3\pi^2}{2}C_q^2(J_1(\omega_0) + 4J_2(2\omega_0)), \qquad (1)$$

$$\frac{1}{T_{1Q}} = \frac{9\pi^2}{2}C_q^2 J_1(\omega_0),$$

where ω_0 is the Larmor frequency, J_1 and J_2 are spectral density functions, and C_q refers to the quadrupole coupling constant in the absence of motion. J_1 and J_2 are dependent on timescales and type of underlying motional processes, as well as on crystallite orientations. Spectral density functions can be obtained analytically for several simple models of motion (63). However, motional models with multiple modes usually require computer simulations.

Three-site jumps of methyl deuterons are usually the main mechanism of relaxation, however other motions of methyl axes can have appreciable contributions as well. Further, the presence of the conformational ensemble in biological molecules and polymers can give rise to distribution of conformers with different rate constants.

We have previously developed a model for protein methyl groups that takes into account the presence of conformers with different rate constants for methyl three-site jumps. Three-site jump motions are usually assumed to follow the Arrhenius behavior for individual conformers. To describe relaxation in a global fashion at all temperatures, we shifted the description to the activation energy space, in which the conformers are distinguished by their unique values of activation energy barrier for three-site jumps E_a.

For a continuous distribution of conformers, the overall observed magnetization $M(t)$ is defined by the following:

$$M(t) = \int m(E_a, t)dE_a, \qquad (2)$$

where $m(E_a, t)$ is the magnetization density in the activation energy space. At equilibrium $m^{eq}(E_a) = M^{eq}f(E_a)$, where $f(E_a)$ is the probability density for the system to be in the state with the activation energy E_a. The distribution of the activation energies is assumed to have a Gaussian form $f(E_a) = (1/\sqrt{2\pi\sigma^2})\exp(-((E_a - \langle E_a\rangle)^2/2\sigma^2))$. The relaxation rate depends on the activation energy through the three-site jump rate constant k_3: $k_3(E_a, T) = k_0 e^{-E_a/T}$. Note, that for a system that follows this model magnetization build-up curves are nonexponential. Nonexponential relaxation decay for ^{2}H nuclei has been observed in multiple polymer systems (64–68), and one of the approaches to parametrize this behavior is to fit the magnetization curve to the stretched-exponential function of the following form:

$$M(t) - M(\infty) = (M(0) - M(\infty))e^{-\left(t/T_1^{eff}\right)^{\beta}}, \qquad (3)$$

in which $M(t)$ is the signal intensity, T_1^{eff} is the effective relaxation time, and β is the parameter that reflects the degree of nonexponentiality, $0 < \beta \leq 1$. β less than 1 corresponds to a nonexponential behavior. Note that for saturation recovery measurements $M(0) = 0$.

Up to this point we have summarized the behavior under the assumption of the absence of conformational exchange between the substates of the conformational ensemble and we refer to this situation as the "static case." However, when the conformational exchange is occurring on the timescale of relaxation time, it has an effect both on the effective relaxation rate and, to a larger extent, on the observed extent of nonexponentiality β. Specifically, we have shown that it slightly lowers the value of T_1^{eff} and significantly raises the value of β. The decay of the longitudinal magnetization in the presence of conformational exchange can be described by Bloch-McConnell equations (69), adapted for the presence of the distribution of conformational states. We have also assumed that short-range stochastic jumps in the activation energy space are the most appropriate description.

Modeling

Leucine residues

The model-predicted values of effective longitudinal relaxation times (T_{1Z}^{eff}) and stretching exponent (β) were found through the simulation of the longitudinal relaxation experiment and fitting the stretched exponential function to the decay curves. For leucine residues the three-site jumps model was used, which requires as its input the jump constant k_3. The deuteron quadrupole constant C_q was fixed at 160 kHz and we assumed the ideal

tetrahedral geometry for the methyl groups. The model parameters comprise the central value for the activation energy $\langle E_a \rangle$, the width of the distribution of activation energies σ, and the Arrhenius law prefactor k_0. We discretized the distribution of activation energies as $E_{a,i} = \langle E_a \rangle + (1/N - 1)(i - (N + 1/2)) \times 6\sigma$ with $i = 1..N$. This creates a uniform grid covering the interval of activation energies $[\langle E_a \rangle - 3\sigma, \langle E_a \rangle + 3\sigma]$ around the central value with interval between the grid points of $\Delta E_a = E_{a,i+1} - E_{a,i} = (6\sigma/N - 1)$. We found it sufficient to use 11 grid points ($N = 11$), but checked that increasing the number of grid points to 21 did not affect the results.

To generate partially relaxed curves for each individual conformer we used the EXPRESS software package (70). This program explicitly allows for simulations of the QCPMG detection scheme. For each temperature point, the three-jump constant for the i^{th} conformer was $k_{3,i}(T) = k_0 e^{-E_{a,i}/RT}$. The overall partially relaxed spectra were obtained as the weighted average of 11 grid points with the weights $f_i \propto \exp[-(E_{a,i} - \langle E_a \rangle)^2/2\sigma^2]$. In analogy to the treatment of the experimental data, resulting spikelet intensities at selected frequencies were fitted to the stretched exponential function of Eq. 3. The model parameters were then found by χ^2 minimization of the difference between experimental and predicted values of $\ln T_{1Z}^{eff}$ and β summed up over all temperatures but the highest two.

At high temperatures deviating from the static case, the exchange between conformers was introduced. Based on the distribution of three-site jump rates at each temperature in the static case, we calculated relaxation times $T_{1Z,i} = T_{1Z}(E_{a,i})$ for each of the conformers and used them in solving the Bloch-McConnell equation in the nearest neighbor approximation as follows:

$$\frac{dm_i}{dt} = -\frac{m_i - m_i^{eq}}{T_{1Z,i}} - k' m_i (f_{i+1} + f_{i-1}) + k' f_i (m_{i+1} + m_{i-1}), \tag{4}$$

where $m_i = m(E_{a,i}, t)$ is the magnetization in each conformer, m_i^{eq} its equilibrium value, f_i are relative weights of the conformers, and k' is the nearest-neighbor jump rate. To obtain a closed system of equations, we set $f_0 = f_{N+1} = 0$ and $m_0 = m_{N+1} = 0$. To describe the rate of the exchange in terms independent of the discretization scheme we introduced k_{ex} constant according to the equation $k_{ex} = (k'/2\sqrt{\pi})(\Delta E_a^3/\sigma^3)$(see (71) for details). The overall magnetization $M(t) = \sum_{i=1}^{N} m_i(t)$ was then approximated by the stretched exponential function and the values of k_{ex} were fixed by fitting experimental and model values. To determine the ranges of k_{ex} values consistent with the experimental data, we used the range of β within one standard deviation.

Methionine

Simulation of relaxation for methionine residues required the use of two motional modes nested within one another. The first mode, three-site jumps, was treated similarly to the leucine residues. C_q of 175 kHz and ideal tetrahedral geometry around the methyl carbon was used (30). The second mode is the diffusion of the methyl axis (S-C^{ε}) along an arc on a side of the cone with the axis along the C^{γ}-S bond (Fig. S2). The two lone pairs of electrons on the sulfur cause deviations from the tetrahedral geometry and thus the angle of the methyl axes with respect to the C^{γ}-S is set to 99° (72). In general, the motion along the arc should be described through a local potential for this degree of freedom. We have previously found (73) that a good assumption is a constant potential on a restricted arc. The diffusion process was simulated by discretizing the orientation of the methyl axis along an arc of angular length α in steps of 1° along the polar angle φ, using nearest neighbors jumps with the rate constant $k_D = D/(\Delta\phi)^2$, where D is the diffusion coefficient. Assuming the Arrhenius temperature dependence of D, the fitting parameters of this mode include the length of arc α and the activation energy and the prefactor for the diffusion constant E_D and D_0, respectively.

The relaxation rates for both Zeeman and quadrupole order were fitted with the EXPRESS software package, which accommodates multimode motions routinely (70). Quadrupolar echo detection scheme was simulated for relaxation at 9.4 T and QCPMG detection was simulated for relaxation at 17.6 T, in accordance with the experiment.

The parameters for the three-site jump motions ($\langle E_a \rangle$, σ, and k_0) as well as for the diffusion constant (E_D and D_0) were ultimately fitted by χ^2 minimization of the difference between experimental and predicted variables, summed over all temperatures and all available experiments. The errors in these fitting parameters were obtained by covariance matrix method. For the case of Zeeman relaxation both experimental and simulated magnetization decay curves were fitted to the stretched-exponential functions yielding T_{1Z}^{eff} and β, whereas quadrupolar order relaxation at high temperature was approximated by single-exponential decay with the relaxation time T_{1Q} due to small extent of nonexponentiality.

The length of the arc α was selected separately as a part of the search of the initial parameters for global minimization. First, we have found approximate values for the parameters of the three-site jumps mode by fitting only the lower temperature range ($T < 250$K) of the T_{1Z} relaxation data and taking into account only this mechanism. We then searched for the values of the arc length and diffusion coefficients at high temperatures ($T > 250$K) by using the full motional model in which the parameters of the three-site jumps mode were projected from these approximate values. For the threefold symmetric hydrated sample, for which relaxation data were available at two values of the magnetic field strength, we found that the value of α can be fixed with little uncertainty. However, for the twofold symmetric and D23N mutant protofibrils in the hydrated state the values of α and diffusion rate constant D could not be found independently of each other and we have chosen to fix α at the value found for the threefold symmetric polymorph. Then, using the chosen value of α, the diffusion constants for the individual higher temperature points were found for all of the hydrated samples (see Supporting Materials and Methods and Fig. S2), from which the initial values of E_D and D_0 were calculated.

RESULTS AND DISCUSSION

As described in detail in Materials and Methods, the samples have been synthesized with selective incorporation of methyl deuteron labels in single residues, therefore our results obtained with static solid-state NMR are site-specific. As demonstrated in Fig. 1, we investigate two hydrophobic core residues L17 and L34 as well as M35, which is essential in defining hydrophobic cavities in the fibril. Further, for each site we investigate and discuss three different variants: the twofold symmetric polymorph, the threefold symmetric polymorph, and the D23N protofibrils. For the wild-type polymorphs, we also investigate the hydration dependence by comparing the behavior in the dry lyophilized fibrils (denoted by "dry") and the hydrated fibrils with 200% incorporation of water by weight (denoted by "wet").

Nonexponential longitudinal relaxation profiles

For signal enhancement, most of the relaxation data have been collected with the multiple-echo acquisition scheme (QCPMG), which breaks the powder pattern into a series of spikes with the distance between the spikes governed

by the echo times. Examples of spectra are shown in Fig. 2. QCPMG detection retains anisotropy of the relaxation rates, which, however, is difficult to quantify for low-sensitivity samples. We report relaxation rates at major singularities, which are ± 10 kHz for leucine side chains and 0 kHz for methionine side chains.

Examples of individual relaxation build-up curves are shown in Fig. 3. Deviations from a simple single-exponential behavior are observed for all sites probed and are significantly more pronounced at lower temperatures. The same tendency has been observed for the hydrophobic core methyl groups of globular villin headpiece subdomain protein (71). We have attributed the nonexponentiality in the villin headpiece protein to the presence of multiple conformers, which are due to some differences in core packing. Since the relaxation rates of methyl groups are dominated by the three-site jump mechanisms, to get the nonexponentiality of the decay curves one must have a distribution of three-site jump rate constants. The distribution of rate constants is very often seen in polymers, in which the resulting relaxation behavior is described as "glassy" (74,75). Longitudinal relaxation measurements over a broad-temperature range thus permit one to probe the "glassiness" in proteins, which is due to much finer differences between the conformers compared with polymers, because large-scale intramolecular motions are not present in the hydrophobic regions of globular proteins. The very fact that the fibrils display similar features already reports on the extent of the conformational heterogeneity, which appears to be similar to what has been observed in the globular villin headpiece. Following the approach developed for polymers (64–68), the build-up curves are fitted to the stretched-exponential function, defined in Eq. 3.

Core residues: leucine-17 and leucine-34

When we fit the relaxation build-up curves at all temperatures according to Eq. 3, we obtain the relaxation profiles depicted in Fig. 4. To describe the conformational ensemble and its effect on the relaxation rates across the entire temperature range, we have developed an approach in which the conformers of the ensemble are distinguished by their activation energy values (71), as summarized in Materials and Methods. Such an approach naturally leads to an increase in nonexponentiality at lower temperatures, because the width distribution in the rate constants on the logarithmic scale, $\ln(k_3)$, is related to the width of distribution of the activation energies by σ/T. The degree of nonexponentiality depends also on the sensitivity of the function $T_{1Z}(E_a)$ to the variation of the activation energy. For example, in the vicinity of the temperature where $T_{1Z}(\langle E_a \rangle)$ approaches its minimum (~195 K for leucine residues), $T_{1Z}(E_a)$ has a weak dependence on E_a and the degree of nonexponentiality of the relaxation profiles decreases, resulting in higher values of β, as one can see in Fig. 4. The fits according to this model are shown by solid lines in Fig. 4. We observe that for the first one or two highest temperatures there are consistent deviations, resulting in higher than predicted values of β

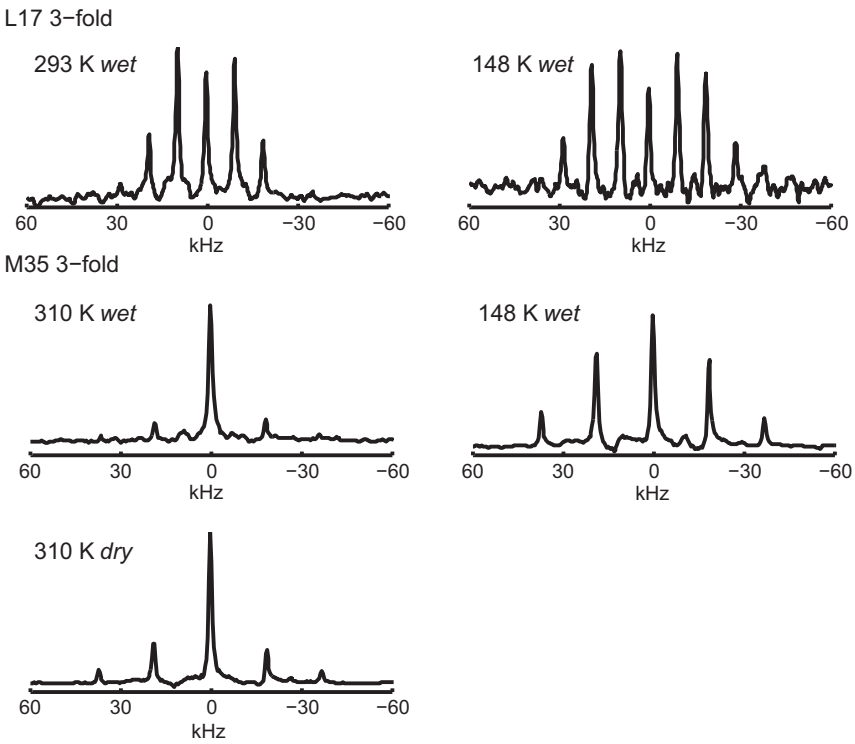

FIGURE 2 Examples of QCPMG spectra corresponding to the largest relaxation delay in the longitudinal relaxation times measurements for L17 and M35 sites in the threefold morphology.

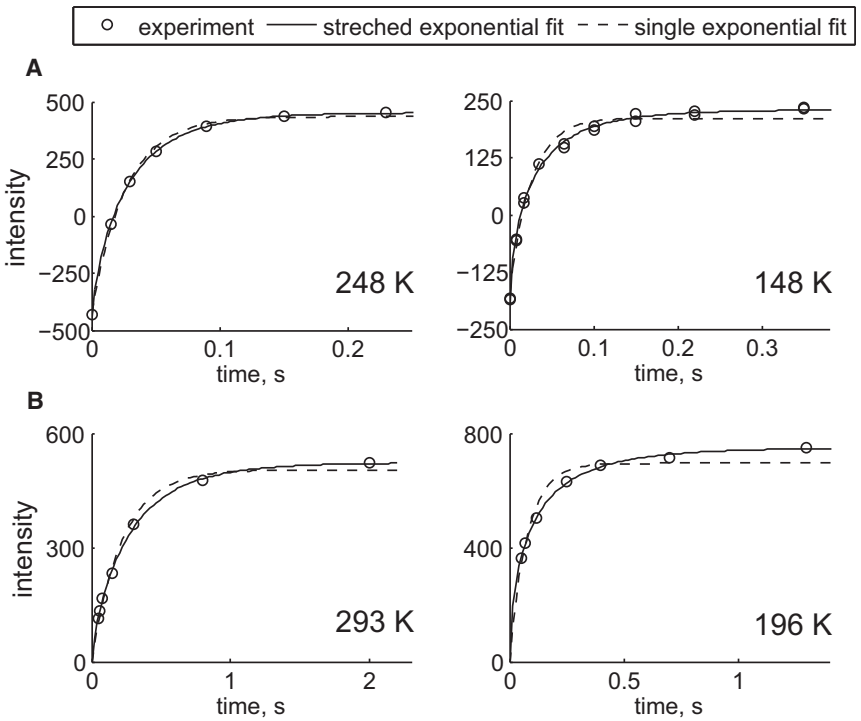

FIGURE 3 Examples of Zeeman relaxation build-up curves M(t) at 17.6 T magnetic field strength for (A) L34 in the twofold polymorph at 248 and 148 K from inversion recovery measurements with intensities taken at ± 10 kHz spikelets, and for (B) M35 in the threefold native polymorph (hydrated state) at 293 and 196 K from saturation recovery with intensities taken at the 0 kHz spikelet. Dashed lines correspond to the best fit mono-exponential decays and solid lines to the best fit stretched-exponential function defined in Eq. 3. Intensity is shown in arbitrary units.

and slightly lower values of T_{1Z}^{eff}. Similarly to the case of villin headpiece protein, this behavior can be attributed to the presence of exchange between the conformers on the timescale of T_{1Z}^{eff}, which is in tenths of milliseconds range.

Fitted parameters of the model, including the estimates of the conformational exchange rate constants are shown in Table 1. First, we see that the central values of activation energies are in 13–16 kJ/mol range, which is typical for globular proteins (37). The twofold morphology has a tendency to have somewhat higher values of E_a than the threefold one, with D23N protofibrils closer to the twofold variant. The widths of the distributions in E_a, which are ~13% from the central values of the activation energies, are rather similar to each other in all polymorphs as well as to the globular villin headpiece. Thus, the variations in packing in the fibrils is similar to globular proteins.

The presence of conformational exchange at high temperatures is seen for all sites with the exception of the L17 twofold. The value of k_{ex} can only be determined quantitatively when it falls within the range given by the following:

$$1/5 < k_{ex} \times T_{1Z}^{eff} < 5. \quad (5)$$

For much lower values of k_{ex} the distribution appears to us as "static," i.e., no exchange. For much higher values of k_{ex}, we can only set the lower limit of the exchange rate constant. Our measurements show that the exchange rates at high temperatures fall into the range defined by Eq. 5 for all samples but L17 twofold. However, relatively large errors in the values of β allow only for determining in which part of this range k_{ex} falls. We determined that it is in the range between tenths of milliseconds to hundreds of milliseconds (Table 1). It is likely that for the L17 twofold site the exchange is present as well but is on the timescale outside the detection window.

Methionine-35

Relaxation behavior of methionine residues is distinct in comparison with the core leucine residues. First, T_{1Z} relaxation minima are shifted to temperature below 145 K, as has also been seen for L-methionine (76). Most importantly, at high temperatures there is a clear leveling of the relaxation curves (Fig. 5) signifying the presence of an additional motional mechanism that dominates relaxation at these temperatures.

To further assess these motions, we have undertaken quadrupolar order relaxation measurements at high temperatures, as well as obtained field-dependence for one of the samples, M35 in the threefold polymorph in the hydrated state. Quadrupolar order relaxation rates, unlike the Zeeman order ones, do not have $2\omega_0$ dependence in the spectral densities (Eq. 1), and thus provide another independent assessment of motional mechanisms. Measurements of the T_{1Q} times at high field have been performed with the QCPMG acquisition scheme, applied here for the first time, to our knowledge, for protein samples. Examples of spectra and decay curves for the ± 10 kHz spikelet are shown in

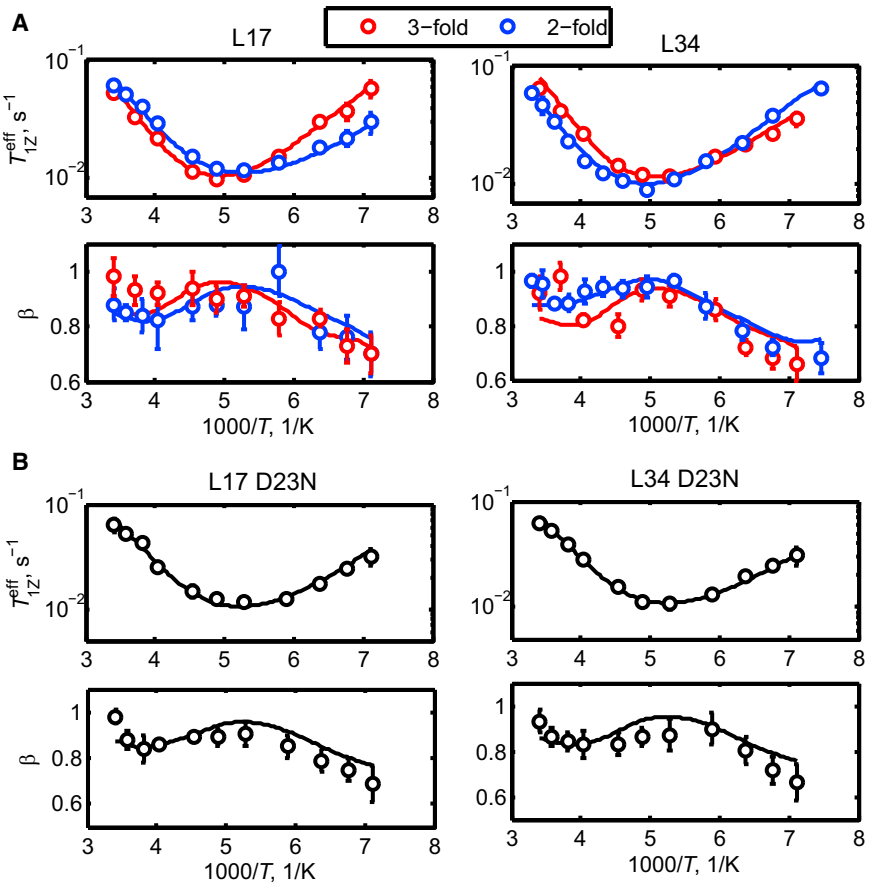

FIGURE 4 Plots of T_{1Z}^{eff} vs. 1000/T on semilog scale and β vs. 1000/T at 17.6 T field strength for L17 and L34 in (*A*) native twofold (*blue*) and threefold (*red*) morphology and (*B*) in the D23N mutant protofibrils. Experimental points (*circles*), fits to the static case model (*solid line*) are shown. Intensities were taken at ± 10 kHz spikelets. Error bars smaller than the size of the symbol are not shown. To see this figure in color, go online.

Fig. 6. In the high-temperature range the expected nonexponentiality of the T_{1Q} relaxation is small and the relaxation decays were fitted with the single-exponential function (Fig. 6) in order not to overfit the data.

Combining both T_{1Z} and T_{1Q} measurements imposes very strict requirements on the choice of the motional model and fitting parameters. Further, the fact that we observe field-dependence for both T_{1Q} and T_{1Z} times indicates that the motions are close to the slow limit with respect to the Larmor frequency. Thus, from a structural standpoint, these motions likely correspond to methyl axis fluctuations. Line shape measurements indicated two types of motions of the methyl axis: large-angle rotameric jumps and diffusion of the methyl axis along a restricted arc of ~30°–35° length, corresponding to motions within rotameric wells. Specifically, the latter mode corresponds to the motions of the S-C$^{\varepsilon}$ axis resulting in changes of the χ_3 dihedral angle within the range of ~35° inside a rotameric well (Fig. S2).

Rotameric jumps have been shown to be in the μs-ms timescale range for our samples by the line shape measurements, and thus are inefficient in causing T_{1Z} and T_{1Q} relaxation as they are too slow with respect to the Larmor frequency. The diffusion constants for the motion along the arc could not be determined from the line shape

TABLE 1 Values of the Fitted Parameters for L17 and L34 Sites

Residue	lnk_0 (s^{-1})	$<E_a>$ (kJ/mol)	σ (kJ/mol)	k_{ex} (s^{-1}) with Ranges in Brackets
L17 twofold	28.0 ± 0.2	13.1 ± 0.3	1.6 ± 0.4	none
L17 threefold	28.6 ± 0.2	14.9 ± 0.3	1.3 ± 0.4	293 K: 202 (34–361)
				270 K: 66 (10–165)
L17 D23N	28.4 ± 0.2	13.8 ± 0.3	1.7 ± 0.4	293 K: 194 (81–600)
L34 twofold	28.1 ± 0.1	14.0 ± 0.3	1.7 ± 0.4	303 K: 43(27–64)
				291 K: 121 (31–510)
L34 threefold	29.4 ± 0.2	15.8 ± 0.4	1.6 ± 0.4	293 K: 99 (38–346)
				270 K: 297 (151–403)
L34 D23N	28.3 ± 0.2	13.6 ± 0.3	1.7 ± 0.4	293 K: 71 (21–240)

Based on the models described in the text. Dry and wet samples are identical.

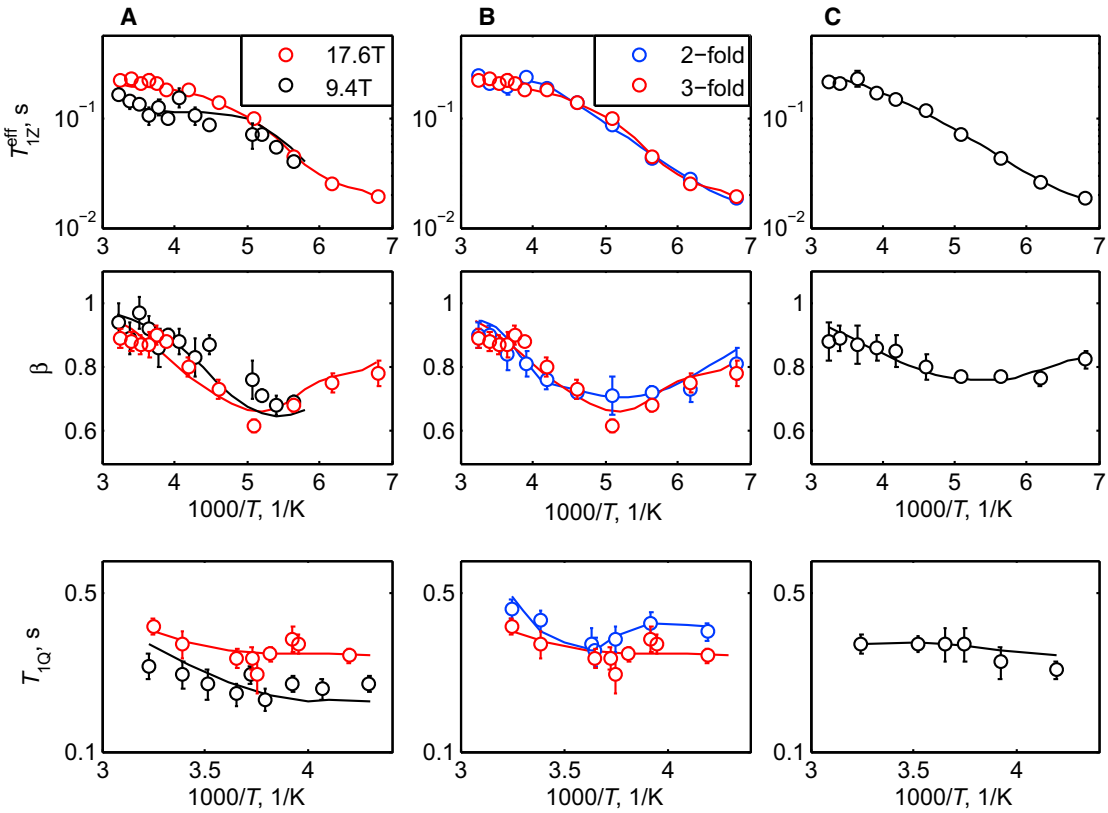

FIGURE 5 Plots of T_{1Z}^{eff} vs. 1000/T on semilog scale, β vs. 1000/T, and T_{1Q} vs. 1000/T on semilog scale for M35 in (*A*) native threefold morphology collected at two different fields of 17.6 T (*red*) and 9.4 T (*black*), (*B*) native twofold (*blue*) and threefold (*red*) polymorphs at 17.6 T, and (*C*) D23N mutant protofibrils at 17.6 T. Intensities were taken at 0 kHz spikelet. Error bars smaller than the size of the symbol are not shown. To see this figure in color, go online.

measurements other than observing that the timescale is much faster compared with the effective quadrupole coupling constant of 58 kHz. Thus, it is likely that the diffusive motion of the methyl axis within rotameric wells is the additional mechanism that is responsible for the leveling of the relaxation curves at high temperatures. We note that the asymmetric diffusive motion along a restricted arc was necessary to explain asymmetry in the line shapes, and, to be consistent with all experimental data, we employed the same mode to explain the relaxation behavior.

As such, overall relaxation behavior is due to an interplay between two motional mechanisms, the three-site jumps dominating at low temperatures and the diffusion of the methyl axes dominating at high temperatures. Each of these mechanism has its own temperature dependence governed by the values of the activation energies E_D and E_a for the diffusion and the three-site jump motions, respectively.

The length of the arc α is best constrained by the field-dependent data (Fig. 7). When the diffusive motion is close to slow motional regime, the absence of the field-dependent data leads to large ambiguities in the value of α, in the sense that there exists a strong correlation between the values of the arc length and the diffusion rate constants. Thus, to facilitate the comparison between the three polymorphs, we fixed α at 34° obtained from the field-dependent data for the M35 hydrated samples in the threefold polymorph, and kept the length the same for the twofold and the D23N hydrated samples.

Quadrupolar order relaxation appears to be more sensitive to the diffusive motion compared with the Zeeman order, thus T_{1Q} measurements were instrumental in detecting differences between the twofold and threefold polymorphs at high temperatures (Figs. 5 and S4). All available rates were fitted together at all temperatures to the two-mode motional model and revealed that whereas the activation energies for the three-site jump motions E_a are similar in all of the methionine-labeled samples, the activation energies E_D for the diffusion motion are very different between the wild-type twofold and threefold polymorphs: 32 ± 4 and 12 ± 3 kJ/mol, respectively. This is an important new result, to our knowledge, distinguishing the dynamics at the M35-site between the twofold and the threefold polymorphs. Although the structural models have shown significant differences at this site, ^{2}H line shape measurements indicated identical dynamics at the μs-ms timescale range, which is dominated by the rotameric jumps. The relaxation measurements point to the fact that local environment at the M35 site creates differences in faster smaller-angle diffusive motions

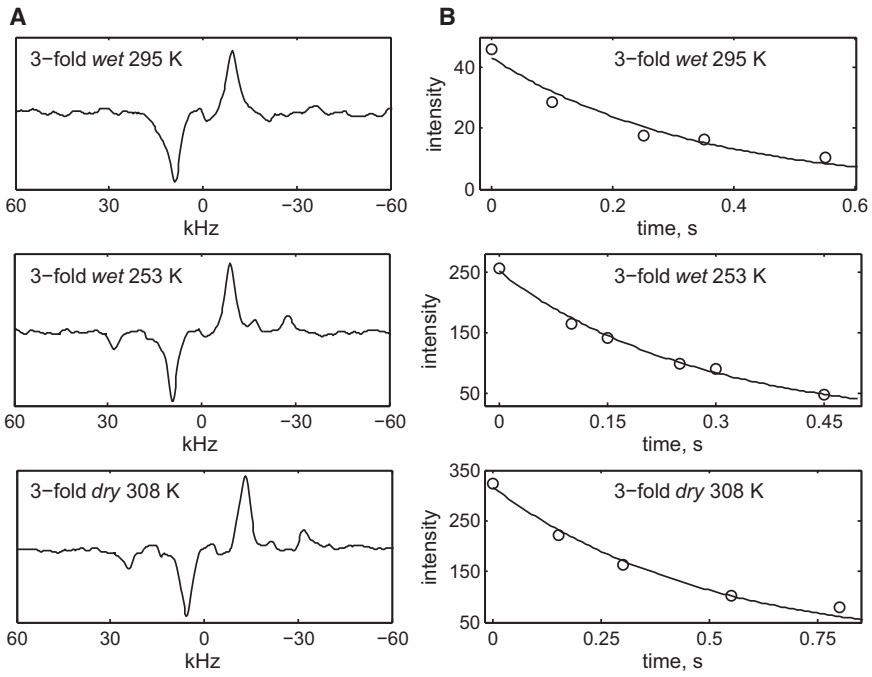

FIGURE 6 (*A*) Examples of spectra for the T_{1Q} measurements at the M35 site corresponding to the shortest relaxation delay of 100 μs. (*B*) Corresponding magnetization decay curves at 17.6 T magnetic field strength taken at $\pm$10 kHz spikelets are shown. Intensity is shown in arbitrary units.

of the methyl axis. The relative differences in the activation energies by a factor of 2.7 provide a measure of the plasticity of the environment at the hydrophobic cavity in the threefold polymorph compared with the twofold one. Interestingly, the value of E_D for the diffusion motions in the D23N protofibrils (9 $\pm$ 2 kJ/mol) is similar to the threefold polymorph. Thus, the environment in the threefold polymorph at the cavity is as flexible as in the monomeric protofibrils, which could be important in designing strategies for drug penetration into the cavity.

The central values of E_a for the three-site jumps are between 7–7.5 kJ/mol (Table 2) for all samples, similar to what has been found for methionine side chains in amino acids (76). The width of the distributions is in the range of 28% to 36%, compared with 13% for the core leucine groups. Thus, the hydrophobic interface has a much larger variability in packing compared with the core regions.

The leveling of the relaxation curves was also observed for L-methionine and one of the methionine residues in methionine-labeled sperm-whale myoglobin, whereas a L-methionine in the D,L lattice as well as another methionine residue in myoglobin did not display this behavior (76). Thus, the fact that the onset of the second motional mode is seen for all M35-labeled samples in Aβ indicates that the local environment around the side chain is flexible enough to accommodate these motions.

Hydration dependence

We have investigated the dependence of relaxation on solvation for the wild-type polymorphs of Aβ. Line shape measurements indicated that L17 and L34 dynamics on the μs-ms timescale is independent of solvation, whereas the M35 site has a strong hydration dependence (30). The following data extend this conclusion to the ps-ns timescale motions.

Relaxation data for the dry and wet samples of the core residues L17 and L34 are indistinguishable (Fig. 8). Unlike

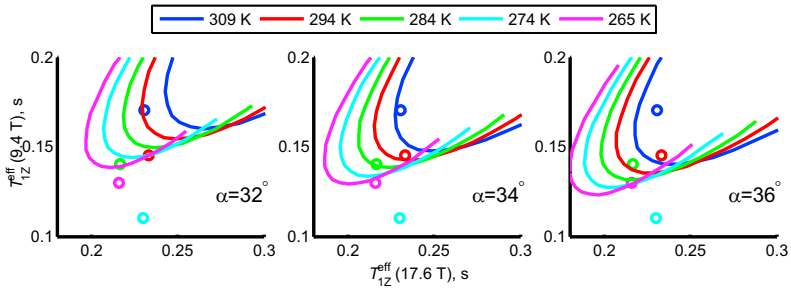

FIGURE 7 Correlation plots of T_{1Z}^{eff} for M35 threefold wet sample at 17.6 T (*horizontal axis*) and 9.4 T (*vertical axis*) for temperatures above 260 K. Solid lines represent simulated values for three fixed arc length values and diffusion coefficients in the range between 1.5 $\times$ 10^6 s^{-1} and 8.0 $\times$ 10^6 s^{-1}, according to the model described in the text. Experimental points (*circles*) are at the following temperatures for 17.6 and 9.4 T, respectively: 307/310 K, 294/295 K, 283/285 K, 274/274 K, and 267/264 K. To see this figure in color, go online.

TABLE 2 Values of the Fitted Parameters for the M35 Sites in the Hydrated State

Polymorph	$\ln k_0$ (s^{-1})	$<E_a>$ (kJ/mol)	σ (kJ/mol)	D_0 (s^{-1})	E_D (kJ/mol)
Twofold	28.0 ± 0.2	7.5 ± 0.6	2.3 ± 0.4	(3.0 ± 0.4) × 10^{12}	32 ± 4
Threefold	28.0 ± 0.2	7.3 ± 0.6	2.6 ± 0.4	(6.5 ± 0.5) × 10^{8}	12 ± 3
D23N	27.4 ± 0.1	7.0 ± 0.5	1.9 ± 0.3	(6.0 ± 0.5) × 10^{7}	9 ± 2

Based on the models described in the text. The value of the arc length was taken as 34° for all polymorphs.

the core residues, M35 displays significant hydration dependence for both the twofold and the threefold polymorphs in the high-temperature range in which the diffusive motions of the methyl axes predominates (Fig. 9). At low temperatures at which the three-site methyl jumps predominate there are no differences between the dry and the wet samples. Interestingly, the dry wild-type fibrils are identical in the twofold and threefold polymorphs (Fig. 9 *B*), indicating that the differences in the dynamics of the two polymorphs are induced by solvation.

Unlike the wet samples, the relaxation data for the dry samples at the M35 site does not require temperature dependence in the diffusion coefficient to fit the high temperature range. Within experimental precision, a constant diffusion coefficient D of ~1.0 × 10^6 s^{-1} to 1.2 × 10^6 s^{-1} can fit all relaxation data in this range, with the length of the arc kept the same at 34°. In comparison, for the wet threefold sample the diffusion coefficient is 6.2 × 10^6 s^{-1} at 310 K and is decreased to 2.6 × 10^6 s^{-1} at 265 K. For the twofold sample, the diffusion coefficient at the physiological temperature is 1.4 × 10^7 s^{-1}. Thus, the main effect of hydration is faster diffusion, with the value of D larger by a factor of 5 to 10 at the physiological temperature.

These new results (to our knowledge) on the hydration dependence combined with the previous line shape measurements are consistent with the existence of the water-accessible cavity around M35 residues, predicted by MD simulations (27). Solvation has an effect of enhancing motions on a wide range of timescales at the M35 site.

The hydration-induced dynamical changes at the M35 site can be interpreted within the framework of the dynamical transitions. As mentioned in the introduction, onset of larger amplitude solvent-dependent modes upon heating from the cryogenic temperatures have been extensively studied for globular proteins, by means of incoherent neutron-scattering, Mössbauer absorption, dielectric spectroscopy, and NMR methods (34,40–43,45,77–83). The crossover temperature between the dominance of smaller-scale faster motional modes at low temperatures and larger-scale slower amplitude modes at high temperatures is usually taken phenomenologically as the change in the slope of a measurable spectroscopic quantity, in our case the relaxation time. The crossover temperature is also often referred to as the "dynamical transition temperature." As can be most clearly seen from Fig. 9 *A*, the threefold hydrated sample experiences the crossover behavior around 250–240 K, at which the diffusive motion becomes dominant. Interestingly, for the twofold sample the transition temperature is in the same range (Fig. 5 *B*, T_{1Z} panel), suggesting perhaps that unfreezing of solvent-related modes is the main driving force in the onset of the diffusion motion. However, the values of the activation energies of these motions are governed by methyl axes environments, which are different in the twofold and threefold fibrils. The dry

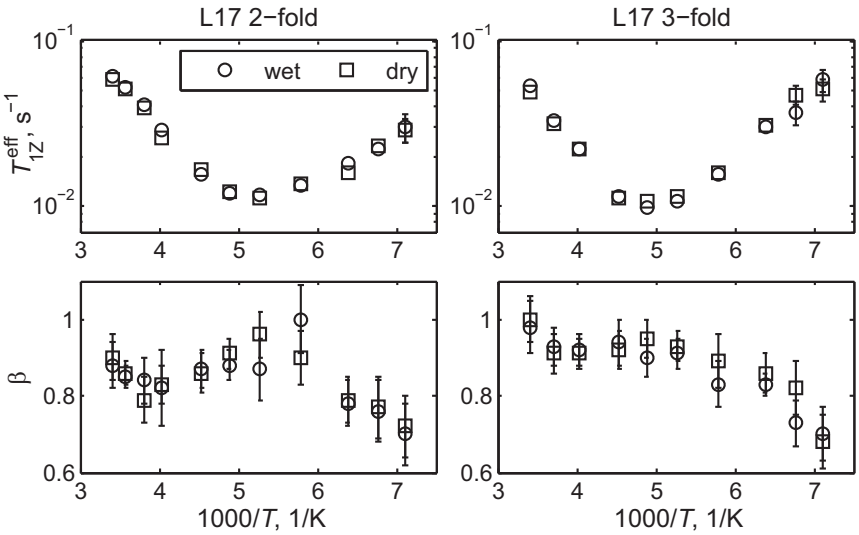

FIGURE 8 Plots of T_{1Z}^{eff} vs. 1000/T and β vs. 1000/T for L17 samples in the twofold and the threefold morphologies in the hydrated (*circles*) and dry (*squares*) states at 17.6 T field strengths. The L34 site shows the same tendency. Error bars smaller than the size of the symbol are not shown.

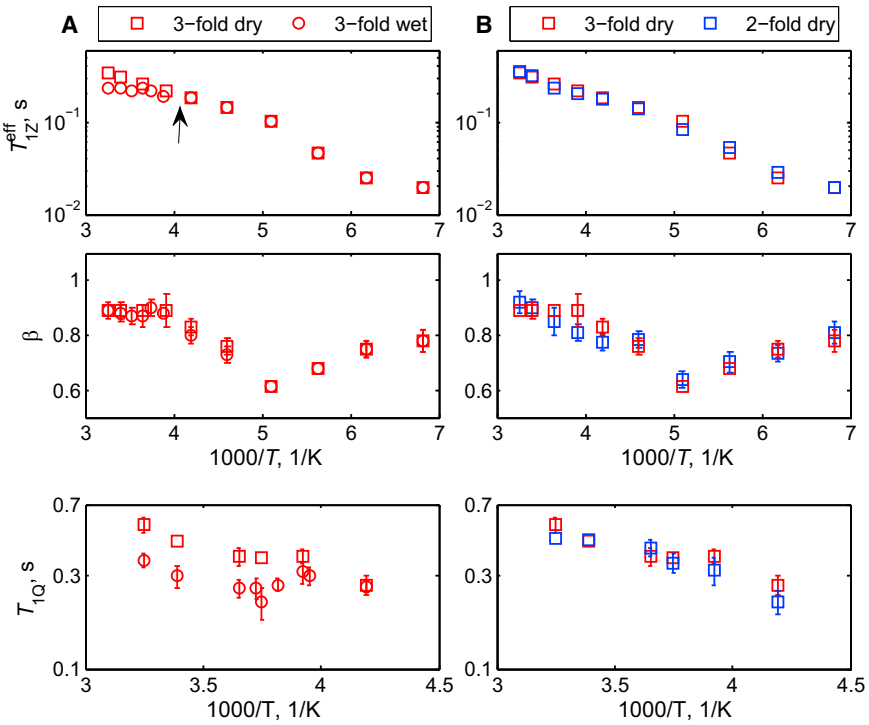

FIGURE 9 Plots of T_{1Z}^{eff}, β, and T_{1Q} vs. 1000/T at 17.6 T magnetic field strength for the M35 site. (*A*) Threefold polymorph in the wet (*red circles*) and dry (*red squares*) states are shown. The arrow indicates the apparent temperature of the dynamical transition in the wet sample. (*B*) The dry state of the twofold (*blue squares*) and threefold (*red squares*) polymorphs are shown. Error bars smaller than the size of the symbol are not shown. To see this figure in color, go online.

samples do not display any significant changes in the apparent slopes of the T_{1Z} relaxation curve, indicating that methyl rotations dominate over a relatively weak diffusive motion even at high temperatures.

CONCLUSIONS

This study has provided several new insights (to our knowledge) into the conformational ensemble of amyloid fibrils and comparison with globular proteins. Fibrils are distinctly different from globular proteins in terms of intra and intermolecular interactions, and thus it is not obvious a priori that features of the conformational ensemble are similar between the two systems.

First, we have seen that hydrophobic core packing and their variations, reflected in the values of the activation energies for methyl rotations and the width of distributions, are similar to packing in globular proteins. Methyl rotations at the core L17 and L34 sites are hydration-independent, again in agreement to what has been observed for the globular proteins (71,84–86). However, the variations in packing at the M35 site, which is outside the core and pointed toward a hydrophobic cavity, is a lot more pronounced, with the width of distribution increased by a factor of two to three. Second, we have observed for the first time, to our knowledge, the features of the dynamical transition in the fibrils. This transition is manifested at the M35 site as an onset of dominance of slower diffusive motions of methyl axis at ~250–240 K, in addition to methyl rotations that dominate at lower temperatures. The diffusive motions are clearly hydration-dependent. It is suppressed in the dry samples, in which methyl rotations remain dominant across the entire range. The results suggest that fibrils may undergo dynamical transitions with activation of not only local, but also more extended large-amplitude modes potentially related to the onset of biological function, in similarity with globular proteins. However, it remains to be seen whether other sites, in particular aromatic residues, solvent-exposed charged side chains, and residues in the unstructured N-terminal also undergo similar dynamical transitions, i.e., that the observed transition is global for the entire fibril.

The diffusive motion of methyl axis at M35 drives the differences between the twofold and threefold symmetric polymorphs. The difference is not observed either at low temperatures (at which methyl rotations predominate) or in the dry states of the two polymorphs. At the physiological temperature, the diffusion coefficient is by a factor of at least five larger for the hydrated samples compared with the dry ones. Combined with the fact that the value of the activation energy for the diffusive motions is almost three time smaller in the threefold polymorph and is comparable with the one detected for the monomeric D23N protofibrils, the results indicate a relatively high degree of flexibility at the hydrophobic cavity. This may be potentially important in the design of drugs targeting the cavity in the more cytotoxic threefold polymorph. The fact that the differences between the two polymorphs at the M35 site are seen only through the motional mode associated with the onset of the dynamical transition, underlies a potential role of the

dynamical transition in the onset of motions distinguishing key features of the two polymorphs.

Our results complement MD studies of the conformational ensemble in amyloid fibrils and open an avenue for the refinement of MD techniques geared toward investigations of the ensemble of various polymorphs across a wide temperature range.

SUPPORTING MATERIAL

Supporting Materials and Methods and four figures are available at http://www.biophysj.org/biophysj/supplemental/S0006-3495(16)30886-4.

AUTHOR CONTRIBUTIONS

L.V. conceived and coordinated the project, designed and performed NMR experiments, and wrote the article with input from all the authors. M.A.C. and I.B.F. prepared the wild-type fibril samples and performed some NMR measurements. D.O. performed modeling with input from L.V. G.L.H. provided NMR resources and technical assistance. W.Q. prepared the D23N mutant fibril samples. All authors discussed the results.

ACKNOWLEDGMENTS

We are grateful to Prof. Robert Tycko for providing fibril seeds and assistance with sample preparation and to Don Gantz for assistance with transmission electron microscopy imaging. We also thank Dr. Riqiang Fu for technical assistance at the National High Magnetic Field Laboratory site.

Support for this research was received from National Institutes of Health Grant 1R15 GM111681-02 to L.V. Some of the experiments were performed at the National High Magnetic Field Laboratory, which is supported by National Science Foundation Cooperative Agreement No. DMR-1157490, the State of Florida, and the U.S. Department of Energy.

SUPPORTING CITATIONS

References (87,88) appear in the Supporting Material.

REFERENCES

1. Ahmed, A. B., and A. V. Kajava. 2013. Breaking the amyloidogenicity code: methods to predict amyloids from amino acid sequence. *FEBS Lett.* 587:1089–1095.
2. Cannon, M. J., A. D. Williams, …, D. G. Myszka. 2004. Kinetic analysis of beta-amyloid fibril elongation. *Anal. Biochem.* 328:67–75.
3. Chimon, S., C. Jones, …, Y. Ishii. 2007. A missing link in amyloid misfolding: structural insights into amyloid intermediates for Alzheimer's beta-amyloid, A beta(1-40) by solid-state NMR. *Biophys. J. (Suppl.)*:195A.
4. Fitzpatrick, A. W. P., G. T. Debelouchina, …, C. M. Dobson. 2013. Atomic structure and hierarchical assembly of a cross-β amyloid fibril. *Proc. Natl. Acad. Sci. USA.* 110:5468–5473.
5. Grabowski, T. J., H. S. Cho, …, S. M. Greenberg. 2001. Novel amyloid precursor protein mutation in an Iowa family with dementia and severe cerebral amyloid angiopathy. *Ann. Neurol.* 49:697–705.
6. Kodali, R., A. D. Williams, …, R. Wetzel. 2010. Aβ (1-40) forms five distinct amyloid structures whose β-sheet contents and fibril stabilities are correlated. *J. Mol. Biol.* 401:503–517.
7. Lewandowski, J. R., P. C. A. van der Wel, …, R. G. Griffin. 2011. Structural complexity of a composite amyloid fibril. *J. Am. Chem. Soc.* 133:14686–14698.
8. Lührs, T., C. Ritter, …, R. Riek. 2005. 3D structure of Alzheimer's amyloid-beta(1-42) fibrils. *Proc. Natl. Acad. Sci. USA.* 102:17342–17347.
9. O'Nuallain, B., S. Shivaprasad, …, R. Wetzel. 2005. Thermodynamics of Aβ(1-40) amyloid fibril elongation. *Biochemistry.* 44:12709–12718.
10. Petkova, A. T., R. D. Leapman, …, R. Tycko. 2005. Self-propagating, molecular-level polymorphism in Alzheimer's beta-amyloid fibrils. *Science.* 307:262–265.
11. Qiang, W., K. Kelley, and R. Tycko. 2013. Polymorph-specific kinetics and thermodynamics of β-amyloid fibril growth. *J. Am. Chem. Soc.* 135:6860–6871.
12. Qiang, W., W. M. Yau, …, R. Tycko. 2012. Antiparallel β-sheet architecture in Iowa-mutant β-amyloid fibrils. *Proc. Natl. Acad. Sci. USA.* 109:4443–4448.
13. Wetzel, R. 2006. Amyloid fibrils—common threads in the natural history of proteins. *Acc. Chem. Res.* 39:567–567.
14. Qiang, W., W. M. Yau, and R. Tycko. 2011. Structural evolution of Iowa mutant β-amyloid fibrils from polymorphic to homogeneous states under repeated seeded growth. *J. Am. Chem. Soc.* 133:4018–4029.
15. Sgourakis, N. G., W. M. Yau, and W. Qiang. 2015. Modeling an in-register, parallel "Iowa" Aβ fibril structure using solid-state NMR data from labeled samples with Rosetta. *Structure.* 23:216–227.
16. Kheterpal, I., A. Williams, …, R. Wetzel. 2001. Structural features of the Aβ amyloid fibril elucidated by limited proteolysis. *Biochemistry.* 40:11757–11767.
17. McDonald, M., H. Box, …, G. Stubbs. 2012. Fiber diffraction data indicate a hollow core for the Alzheimer's Aβ 3-fold symmetric fibril. *J. Mol. Biol.* 423:454–461.
18. Pinotsi, D., A. K. Buell, …, C. F. Kaminski. 2013. A label-free, quantitative assay of amyloid fibril growth based on intrinsic fluorescence. *ChemBioChem.* 14:846–850.
19. Popova, L. A., R. Kodali, …, I. K. Lednev. 2010. Structural variations in the cross-beta core of amyloid beta fibrils revealed by deep UV resonance Raman spectroscopy. *J. Am. Chem. Soc.* 132:6324–6328.
20. Sachse, C., M. Fändrich, and N. Grigorieff. 2008. Paired beta-sheet structure of an Aβ (1-40) amyloid fibril revealed by electron microscopy. *Proc. Natl. Acad. Sci. USA.* 105:7462–7466.
21. Hou, L., H. G. Lee, …, M. G. Zagorski. 2013. Modification of amyloid-$\beta_{1\text{-}42}$ fibril structure by methionine-35 oxidation. *J. Alzheimers Dis.* 37:9–18.
22. Schütz, A. K., T. Vagt, …, B. H. Meier. 2015. Atomic-resolution three-dimensional structure of amyloid β fibrils bearing the Osaka mutation. *Angew. Chem. Int. Ed. Engl.* 54:331–335.
23. Prade, E., H. J. Bittner, …, B. Reif. 2015. Structural mechanism of the interaction of Alzheimer disease Aβ fibrils with the non-steroidal anti-inflammatory drug (NSAID). *J. Biol. Chem.* 290:28737–28745.
24. Linser, R., R. Sarkar, …, B. Reif. 2014. Dynamics in the solid-state: perspectives for the investigation of amyloid aggregates, membrane proteins and soluble protein complexes. *J. Biomol. NMR.* 59:1–14.
25. Hubin, E., N. A. J. van Nuland, …, K. Pauwels. 2014. Transient dynamics of Aβ contribute to toxicity in Alzheimer's disease. *Cell. Mol. Life Sci.* 71:3507–3521.
26. Zhang, R., X. Hu, …, J.-M. Lee. 2009. Interprotofilament interactions between Alzheimer's A$\beta_{1\text{-}42}$ peptides in amyloid fibrils revealed by cryoEM. *Proc. Natl. Acad. Sci. USA.* 106:4653–4658.
27. Miller, Y., B. Ma, and R. Nussinov. 2011. The unique Alzheimer's β-amyloid triangular fibril has a cavity along the fibril axis under physiological conditions. *J. Am. Chem. Soc.* 133:2742–2748.
28. Zheng, J., H. Jang, …, R. Nussinov. 2007. Modeling the Alzheimer A$\beta_{17\text{-}42}$ fibril architecture: tight intermolecular sheet-sheet association and intramolecular hydrated cavities. *Biophys. J.* 93:3046–3057.

29. Prade, E., C. Barucker, …, B. Reif. 2016. Sulindac sulfide induces the formation of large oligomeric aggregates of the Alzheimer's disease amiloid-β peptide which exhibit reduced neurotoxicity. *Biochemistry.* 55:1839–1849.

30. Vugmeyster, L., M. A. Clark, …, G. L. Hoatson. 2016. Flexibility and solvation of amyloid-β hydrophobic core. *J. Biol. Chem.* 291:18484–18495.

31. Vugmeyster, L., D. Ostrovsky, …, R. L. Vold. 2011. Slow motions in the hydrophobic core of chicken villin headpiece subdomain and their contributions to configurational entropy and heat capacity from solid-state deuteron NMR measurements. *Biochemistry.* 50:10637–10646.

32. Igumenova, T. I., K. K. Frederick, and A. J. Wand. 2006. Characterization of the fast dynamics of protein amino acid side chains using NMR relaxation in solution. *Chem. Rev.* 106:1672–1699.

33. Krushelnitsky, A., and D. Reichert. 2005. Solid-state NMR and protein dynamics. *Prog. Nucl. Magn. Reson. Spectrosc.* 47:1–25.

34. Lee, A. L., and A. J. Wand. 2001. Microscopic origins of entropy, heat capacity and the glass transition in proteins. *Nature.* 411:501–504.

35. Mittermaier, A. K., and L. E. Kay. 2009. Observing biological dynamics at atomic resolution using NMR. *Trends Biochem. Sci.* 34:601–611.

36. Vold, R. L., and R. R. Vold. 1991. Deuterium relaxation in molecular solids. *In* Advances in Magnetic and Optical Resonance. W. Warren, editor. Academic Press, San Diego, CA, pp. 85–171.

37. Xue, Y., M. S. Pavlova, …, N. R. Skrynnikov. 2007. Methyl rotation barriers in proteins from 2H relaxation data. Implications for protein structure. *J. Am. Chem. Soc.* 129:6827–6838.

38. Meints, G. A., P. A. Miller, …, G. Drobny. 2008. Solid-state nuclear magnetic resonance spectroscopy studies of furanose ring dynamics in the DNA *Hha*I binding site. *J. Am. Chem. Soc.* 130:7305–7314.

39. McDermott, A., and T. Polenova. 2007. Solid state NMR: new tools for insight into enzyme function. *Curr. Opin. Struct. Biol.* 17:617–622.

40. Doster, W. 2008. The dynamical transition of proteins, concepts and misconceptions. *Eur. Biophys. J.* 37:591–602.

41. Lewandowski, J. R., M. E. Halse, …, L. Emsley. 2015. Protein dynamics. Direct observation of hierarchical protein dynamics. *Science.* 348:578–581.

42. Khodadadi, S., S. Pawlus, …, A. P. Sokolov. 2008. The origin of the dynamic transition in proteins. *J. Chem. Phys.* 128:195106.

43. Magazù, S., F. Migliardo, and A. Benedetto. 2011. Puzzle of protein dynamical transition. *J. Phys. Chem. B.* 115:7736–7743.

44. Vugmeyster, L., D. Ostrovsky, …, R. L. Vold. 2015. Dynamics of hydrophobic core phenylalanine residues probed by solid-state deuteron NMR. *J. Phys. Chem. B.* 119:14892–14904.

45. Halle, B. 2004. Biomolecular cryocrystallography: structural changes during flash-cooling. *Proc. Natl. Acad. Sci. USA.* 101:4793–4798.

46. Khodadadi, S., J. E. Curtis, and A. P. Sokolov. 2011. Nanosecond relaxation dynamics of hydrated proteins: water versus protein contributions. *J. Phys. Chem. B.* 115:6222–6226.

47. Hong, L., X. Cheng, …, J. C. Smith. 2012. Surface hydration amplifies single-well protein atom diffusion propagating into the macromolecular core. *Phys. Rev. Lett.* 108:238102.

48. Wood, K., F. X. Gallat, …, F. A. A. Mulder. 2013. Protein surface and core dynamics show concerted hydration-dependent activation. *Angew. Chem. Int. Ed. Engl.* 52:665–668.

49. Hong, L., N. Smolin, …, J. C. Smith. 2011. Three classes of motion in the dynamic neutron-scattering susceptibility of a globular protein. *Phys. Rev. Lett.* 107:148102.

50. Khodadadi, S., A. Malkovskiy, …, A. P. Sokolov. 2010. A broad glass transition in hydrated proteins. *Biochim. Biophys. Acta.* 1804:15–19.

51. Rasmussen, B. F., A. M. Stock, …, G. A. Petsko. 1992. Crystalline ribonuclease A loses function below the dynamical transition at 220 K. *Nature.* 357:423–424.

52. Ringe, D., and G. A. Petsko. 2003. The 'glass transition' in protein dynamics: what it is, why it occurs, and how to exploit it. *Biophys. Chem.* 105:667–680.

53. Huang, T. H., R. P. Skarjune, …, E. Oldfield. 1980. Restricted rotational isomerization in polymethylene chains. *J. Am. Chem. Soc.* 102:7377–7379.

54. Elkins, M. R., T. Wang, …, M. Hong. 2016. Structural polymorphism of Alzheimer's β-amiloid fibrils as controlled by an E22 switch: a solid-state NMR study. *J. Am. Chem. Soc.* 138:9840–9852.

55. Colvin, M. T., R. Silvers, …, R. G. Griffin. 2016. Atomic resolution structure of monomorphic Aβ_{42} amiloid fibrils. *J. Am. Chem. Soc.* 138:9663–9674.

56. Petkova, A. T., W. M. Yau, and R. Tycko. 2006. Experimental constraints on quaternary structure in Alzheimer's beta-amyloid fibrils. *Biochemistry.* 45:498–512.

57. Hoatson, G. L. 1991. Broadband composite excitation sequences for creating quadrupolar order in 2 H NMR. *J. Magn. Reson.* 94:152–159.

58. Wimperis, S. 1990. Broadband and narrowband composite excitation sequences. *J. Magn. Reson.* 86:46–59.

59. Larsen, F. H., H. J. Jakobsen, …, N. C. Nielsen. 1998. High-field QCPMG-MAS NMR of half-integer quadrupolar nuclei with large quadrupole couplings. *Mol. Phys.* 95:1185–1195.

60. Vold, R. L., G. L. Hoatson, …, P. J. De Castro. 2009. Solid state deuteron relaxation time anisotropy measured with multiple echo acquisition. *Phys. Chem. Chem. Phys.* 11:7008–7012.

61. Beckmann, P. A., and C. Dybowski. 2000. A thermometer for nonspinning solid-state NMR spectroscopy. *J. Magn. Reson.* 146:379–380.

62. Duer, M. J. 2004. Solid-State NMR Spectroscopy. Blackwell Publishing, Oxford, UK.

63. Torchia, D. A., and A. Szabo. 1982. Spin-lattice relaxation in solids. *J. Magn. Reson.* 49:107–121.

64. Schnauss, W., F. Fujara, …, H. Sillescu. 1990. Nonexponential ^{2}H spin-lattice relaxation as a signature of the glassy state. *Chem. Phys. Lett.* 166:381–384.

65. Roggatz, I., E. Rossler, …, R. Richert. 1996. Nonexponential ^{2}H spin-lattice relaxation and slow translational exchange in disordered systems. *J. Phys. Chem.* 100:12193–12198.

66. Schnauss, W., F. Fujara, and H. Sillescu. 1992. The molecular-dynamics around the glass-transition and in the glassy state of molecular organic-systems: a H-2-nuclear magnetic-resonance study. *J. Chem. Phys.* 97:1378–1389.

67. Roessler, E., M. Taupitz, and H. M. Vieth. 1990. Heterogeneous spin-lattice relaxation revealing the activation-energy distribution of mobile guests in organic glasses. *J. Phys. Chem.* 94:6879–6884.

68. Beckmann, P. A., and E. Schneider. 2012. Methyl group rotation, 1H spin-lattice relaxation in an organic solid, and the analysis of nonexponential relaxation. *J. Chem. Phys.* 136:054508.

69. McConnell, H. M. 1958. Reaction rates by nuclear magnetic resonance. *J. Chem. Phys.* 28:430–431.

70. Vold, R. L., and G. L. Hoatson. 2009. Effects of jump dynamics on solid state nuclear magnetic resonance line shapes and spin relaxation times. *J. Magn. Reson.* 198:57–72.

71. Vugmeyster, L., D. Ostrovsky, …, R. L. Vold. 2013. Glassy dynamics of protein methyl groups revealed by deuteron NMR. *J. Phys. Chem. B.* 117:1051–1061.

72. Haynes, W. M., and D. R. Lide. 2011. CRC Handbook of Chemistry and Physics. CRC Press, Boca Raton, FL.

73. Vugmeyster, L., D. Ostrovsky, …, R. L. Vold. 2009. Probing the dynamics of a protein hydrophobic core by deuteron solid-state nuclear magnetic resonance spectroscopy. *J. Am. Chem. Soc.* 131:13651–13658.

74. Sillescu, H. 1999. Heterogeneity at the glass transition: a review. *J. NonCryst. Sol.* 243:81–108.

75. Böhmer, R., G. Diezemann, …, E. Rössler. 2001. Dynamics of supercooled liquids and glassy solids. *Prog. Nucl. Magn. Reson.* 39:191–267.

76. Keniry, M. A., T. M. Rothgeb, …, E. Oldfield. 1983. Nuclear magnetic resonance studies of amino acids and proteins. Side-chain mobility of methionine in the crystalline amino acid and in crystalline sperm whale (*Physeter catodon*) myoglobin. *Biochemistry.* 22:1917–1926.

77. Kaempf, K., B. Kremmling, and M. Vogel. 2014. Vanishing amplitude of backbone dynamics causes a true protein dynamical transition: H-2 NMR studies on perdeuterated C-phycocyanin. *Phys. Rev. E Stat. Nonlin. Soft Matter Phys.* 89:032710.

78. Doster, W. 2006. Dynamical structural distributions in proteins. *Physica B.* 385–386:831–834.

79. Capaccioli, S., K. L. Ngai, …, A. Paciaroni. 2012. Evidence of coexistence of change of caged dynamics at T(g) and the dynamic transition at T(d) in solvated proteins. *J. Phys. Chem. B.* 116:1745–1757.

80. Kim, C. U., M. W. Tate, and S. M. Gruner. 2011. Protein dynamical transition at 110 K. *Proc. Natl. Acad. Sci. USA.* 108:20897–20901.

81. Abergel, D., and G. Bodenhausen. 2005. Predicting internal protein dynamics from structures using coupled networks of hindered rotators. *J. Chem. Phys.* 123:204901.

82. Chong, S. H., Y. Joti, …, F. Parak. 2001. Dynamical transition of myoglobin in a crystal: comparative studies of x-ray crystallography and Mössbauer spectroscopy. *Eur. Biophys. J.* 30:319–329.

83. Miao, Y., Z. Yi, …, J. C. Smith. 2012. Temperature-dependent dynamical transitions of different classes of amino acid residue in a globular protein. *J. Am. Chem. Soc.* 134:19576–19579.

84. Roh, J. H., V. N. Novikov, …, A. P. Sokolov. 2005. Onsets of anharmonicity in protein dynamics. *Phys. Rev. Lett.* 95:038101.

85. Krishnan, M., V. Kurkal-Siebert, and J. C. Smith. 2008. Methyl group dynamics and the onset of anharmonicity in myoglobin. *J. Phys. Chem. B.* 112:5522–5533.

86. Khodadadi, S., and A. P. Sokolov. 2015. Protein dynamics: from rattling in a cage to structural relaxation. *Soft Matter.* 11:4984–4998.

87. Harris, J. R., and J. W. Horne. 1991. Negative staining. *In* Electron Microscopy in Biology. J. R. Harris, editor. IRL Press, Oxford, UK, pp. 203–228.

88. Dubochet, J., M. Groom, and S. Mueller-Neuteboom. 1982. The mounting of macromolecules for electron microscopy with particular reference to surface phenomena and the treatment of support films by glow discharge. *Adv. Opt. Electron Microsc.* 8:107–135.